PSFC/JA-12-5

A new model to account for track overlap in CR-39 data.

Zylstra, A.B., Frenje, J.A., Séguin, F.H., Gatu Johsnon, M., Casey, D.T., Rosenberg, M.J., Waugh, C., Sinenian, N., Manuel, M.J.-E., Li, C.K., Petrasso, R.D., Kim, Y.*, Herrmann, H.W.*

* Los Alamos National Laboratory

February 2012

Plasma Science and Fusion Center
Massachusetts Institute of Technology
Cambridge MA 02139 USA

This work was supported was supported in part by the U.S. DoE (DE-FG52-09NA29553), LLNL (B580243), LLE (414090-G), the Fusion Science Center at the University of Rochester (415023-G), and the National Laser Users Facility (DE-NA0000877). A. Zylstra is supported by the DoE NNSA Stewardship Science Graduate Fellowship (DE-FC52-08NA28752).

A new model to account for track overlap in CR-39 data

A. B. Zylstra, J. A. Frenje, F. H. Séguin, M. Gatu Johnson, D. T. Casey, M. J. Rosenberg, C. Waugh, N. Sinenian, M. J.-E. Manuel, C. K. Li, R. D. Petrasso

Plasma Science and Fusion Center, Massachusetts Institute of Technology, Cambridge, MA 02139, USA

Y. Kim, H. W. Herrmann

Los Alamos National Laboratory, Los Alamos, New Mexico 87545, USA

Abstract

The solid-state nuclear track detector CR-39 is widely used as a detecting mechanism in physics experiments as well as for industrial purposes such as neutron dosimetry and radon detection. The upper limit of detectable charged-particle fluence on CR-39 is set by physical overlapping or 'pulse pileup' of particle tracks on the surface. In the low-overlap regime the overlapping fraction of tracks scales as $\chi \equiv \eta \times (\pi \bar{D}^2)$ where η is the density of tracks and $\bar{D}$ is the average track diameter. We report on the development of a Monte Carlo simulation to predict the severity of track overlap for any fluence of an arbitrary diameter distribution of tracks. Furthermore, we present an algorithm to correct for particle-track overlap in a post-hoc manner based on these Monte Carlo simulations, which can extend the upper fluence limit for a quasi-monoenergic source by a factor of $3-4$ when counting accuracies $\sim 10\%$ are acceptable.

Keywords:
CR-39, Nuclear track detectors, Inertial Confinement Fusion

1. Introduction

Solid-state nuclear track detectors have been developed for several decades[1, 2, 3, 4]. CR-39 itself was developed as a nuclear track detector starting in the 1980s[5]. Significant work characterizing the response of CR-39 has been published in the last three decades; a recent comprehensive paper on the response of CR-39 to protons has been published by Sinenian et al. along with a comprehensive bibliography of studies on CR-39[6]. Of particular interest to this work is that CR-39 is widely used in modern Inertial Confinement Fusion (ICF) [7] experiments due to its 100% charged particle detection efficiency[1] and relative insensitivity to electromagnetic pulse (EMP) and x-ray irradiation. The first use of this detector was to measure fuel areal density [8]; recent experiments have used CR-39 for charged-particle spectroscopy [9, 10, 11, 12], neutron diagnostics [13, 14], and charged-particle radiography [15, 16, 17]. In many of these applications at modern ICF facilities such as OMEGA [18] or the National Ignition Facility (NIF) [19], charged-particle fluxes of $10^5 - 10^7$ cm^{-2} are possible or expected. As typically a few percent of particle tracks are observed to overlap at track densities of order 10^4 cm^{-2}, these are well into the current saturation regime. For example, an image of CR-39 exposed to 1.8×10^5 protons/cm^2 is shown in Fig. 1, which clearly shows significant track overlap. Recent work has been published on CR-39 data in extremely high fluence environments, such as short-pulse laser ion acceleration [20, 21].

Extending the upper fluence limit of CR-39 would allow: high-contrast charged-particle spectroscopy (e.g. simultaneous measurements of fusion products with reactivities differing by orders of magnitude), higher

Email address: zylstra@mit.edu (A. B. Zylstra)

[1] For a characteristic energy range; for protons this is $\sim 1 - 8$ MeV.

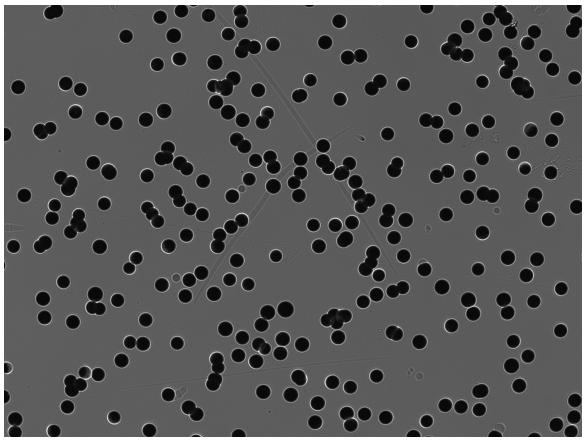

Figure 1: High-fluence, 1.8×10^5 tracks/cm^2 of 3 MeV DD-p, CR-39 with significant overlap observable after being etched for 6 hours. The average track diameter is 10.63μm with a standard deviation of 0.54μm. The image was taken with an optical microscope system with a frame area of 1.36×10^{-3} cm^2 (431μm $\times$ 315.5μm).

signal-to-background neutron spectroscopy of ignited implosions through increased allowable instrument efficiency, higher-contrast proton radiography of mass and EM field distributions, and simple extensions of various existing CR-39 based diagnostics to higher yields. These potential applications clearly motivate development of methods to operate CR-39 detectors into track-overlap saturation regimes, which is quantitatively addressed in this paper.

In addition to the modeling work, experimental data is presented in this paper from CR-39 diagnostics used on implosions at the OMEGA laser facility[18] and from the MIT Linear Electrostatic Ion Accelerator (LEIA)[22, 23].

The structure of this paper is as follows. Section 2 presents an analytic model of track overlap and a convenient dimensionless parameter to describe the amount of overlap, Section 3 discusses the Monte Carlo code developed to model track overlap, Section 4 presents some simulated results, Section 5 describes a post-hoc algorithm to correct for overlap in data, which is tested experimentally. Finally, the paper is concluded in Section 6.

2. Analytic model of track overlap

A complete recurrence-relation model of mono-energetic tracks has been derived [24]. For our purposes it is sufficient to present an integral equation model for single and double tracks at low densities, which illustrates important scalings. This model can be derived by first defining probabilities for a new track being single, double, etc. Let η be the total density of tracks. Then,

$$P_1(\eta) = 1 - \sum_{i=1}^{\infty} \bar{A}_i N_i \tag{1}$$

$$P_n(\eta) = \bar{A}_{n-1} N_{n-1}, \quad n > 1 \tag{2}$$

where P_i is the probability that a new particle track on the detector will have an 'overlap fraction' i(where $i = 1$ is a single track, $i = 2$ is two tracks overlapping each other, $i = 3$ is a cluster of three mutually overlapping tracks, etc).$\bar{A}_i$ is the cross-section of a track, i.e. the area in which a new particle track will overlap with it (see Fig. 2), with overlap fraction i and N_i is the density of tracks with overlap fraction i.

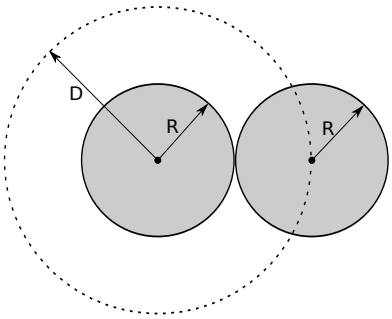

Figure 2: Of relevance for track overlap calculations is the effective cross-section of a track for another track to overlap with it. As illustrated in the figure, for tracks of radius R any track lying within a one diameter separation overlaps, thus $\bar{A}_1 = \pi\bar{D}^2$.

Now assume that $N_i = 0 \ \ \forall \ \ i > 2$. We can write the two probabilities as

$$P_1(\eta) = 1 - \bar{A}_1 N_1 - \bar{A}_2 N_2, \tag{3}$$

$$P_2(\eta) = \bar{A}_1 N_1. \tag{4}$$

Therefore using Eqs 1 and 2 with 3 and 4,

$$N_1(\eta) = \int_0^\eta (P_1(\eta') - P_2(\eta'))d\eta' = \eta(1 - \bar{A}_1\eta), \tag{5}$$

$$N_2(\eta) = \int_0^\eta 2P_2(\eta')d\eta' = \bar{A}_1\eta^2(1 - \frac{2}{3}\bar{A}_1\eta), \tag{6}$$

where in Eq. 5 we have approximated $2\bar{A}_1 N_1 + \bar{A}_2 N_2 \approx 2\bar{A}_1\eta$, neglecting second-order geometric effects of double tracks, to simplify integration for N_1. The factor of 2 in the latter equation results from the fact that a newly-placed track which hits an existing track results in two tracks with overlap fraction 2. The overlap fraction F is defined as

$$F_i(\eta) = N_i(\eta)/\eta. \tag{7}$$

So for an average[2] track diameter $\bar{D}$, we have $\bar{A}_1 = \pi\bar{D}^2$ and if we define the dimensionless parameter $\chi \equiv \eta \times (\pi\bar{D}^2)$,

$$F_1(\chi) = 1 - \chi \tag{8}$$

$$F_2(\chi) = \chi\,(1 - 2\chi/3) \tag{9}$$

This model is plotted as a function of χ versus a full Monte Carlo simulation in Fig. 3, which shows that the analytic model is accurate for overlap fractions up to $\sim 25\%$ (here, track densities up to $\sim 8 \times 10^4/\mathrm{cm}^2$).

The analytic model can be used to estimate amounts of overlap in various diagnostic scenarios. In particular, we consider here the NIF Magnetic Recoil Spectrometer (MRS) [25], which must diagnose a range of implosions from dud THD tuning-campaign implosions ($\mathrm{Y_n} \sim 10^{14}$) to ignited, burning plasmas ($\mathrm{Y_n} \sim 10^{19}$). For example, a break-even NIF implosion has $Y_n \sim 10^{18}$. Since the amount of overlap strongly depends on the average track diameter (Eqs 5 and 6) we vary the track diameter and plot the counting error due to overlap versus the primary neutron yield in Fig. 4. At diameters $1 - 2\mu$m the data would be

[2]Since the track area $\propto D^2$ this is only valid in the limit where the distribution width σ obeys $\sigma/D \ll 1$. For wide distributions the overlap is more heavily weighted towards the higher diameter part of the distribution. In Fig. 8, we see that $\sigma/D \leq 0.3$ has no effect on overlap calculations.

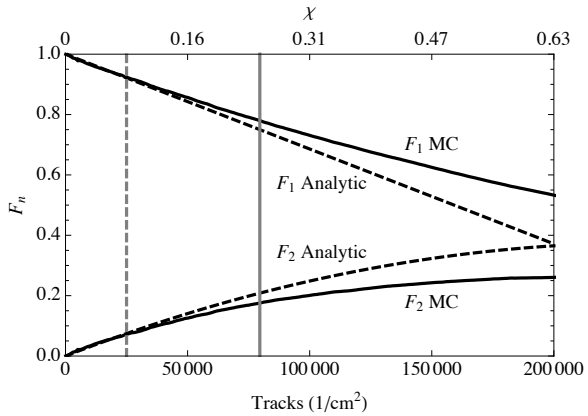

Figure 3: Comparison of Monte Carlo F_1 and F_2 (solid lines) to the analytic model for F_1 and F_2 (dashed lines). The track diameter is 10 μm, the models are plotted versus track fluence and χ. The analytic model begins to fail for $\chi \sim 0.25$, indicated by the solid vertical gray line. Typical track fluences are ≤ 25000, indicated by the dashed vertical gray line. The Monte Carlo statistics are good enough that scatter is not visible on this scale.

indistinguishable from intrinsic noise in the CR-39, placing a lower limit on the fluence dynamic range gain achievable with short etch times.

This information can also be plotted as the maximum allowable yield versus track diameter, Fig. 5. This is calculated for six MRS configurations; in high-yield implosions the efficiency can be reduced to avoid track overlap via thinner foils and smaller apertures, but this has the undesirable effect of simultaneously lowering the signal-to-background ratio.

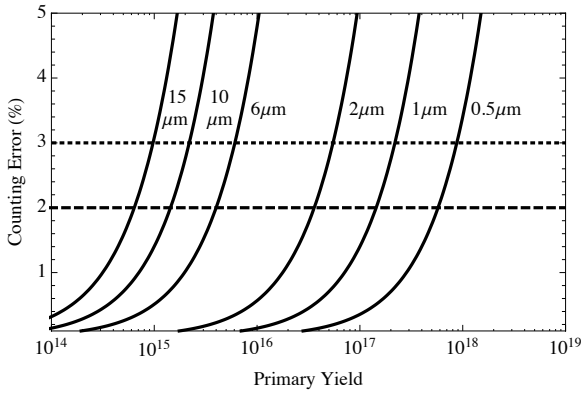

Figure 4: Counting error due to track overlap versus primary neutron yield for a variety of track diameters ($0.5 - 15\mu$m). This is calculated for the NIF Magnetic Recoil Spectrometer (MRS) efficiency using a 20 cm^2 aperture and 138.2μm CD foil. The dashed and dotted lines represent $2 - 3\%$ counting error, the maximum allowable error for this application.

3. Simulation code

A Monte Carlo track overlap code has been developed for computational studies of this problem. The code randomly places tracks using a uniform spatial distribution in the simulation plane. Track diameters

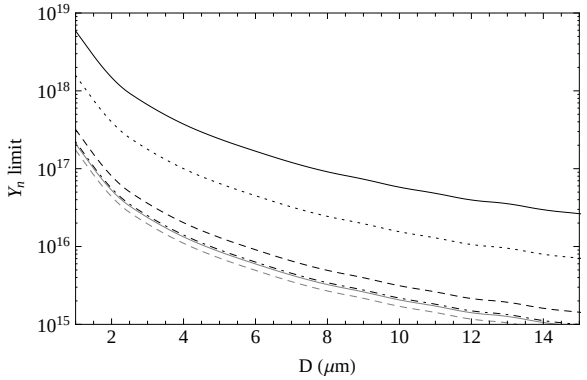

Figure 5: Using the results of Fig. 4, the allowable Y_n for a 3% counting error is plotted versus track diameter for the NIF MRS efficiency using a the configurations in Table 1, from top to bottom: solid (#1), dotted (#2), dashed (#3), dot-dashed (#4), solid gray (#5), and dashed gray (#6).

Number	Foil (μm)	Aperture (cm^2)	Efficiency [Tracks/(DT-n cm^2)]
1	25	1	3.24×10^{-13}
2	25	6	1.21×10^{-12}
3	47.4	20	5.98×10^{-12}
4	100.4	20	8.61×10^{-12}
5	138.2	20	9.1×10^{-12}
6	259.2	20	1.1×10^{-11}

Table 1: MRS Configurations, with calculated efficiency (signal + background). Configurations 3-6 are currently in use at the NIF.

are chosen from Gaussian or arbitrary distributions. The code incrementally adds a number of tracks dN and computes the overlap fractions at each step. A buffer region outside of the proper simulation area ensures accurate counting without edge effects (see Fig. 6).

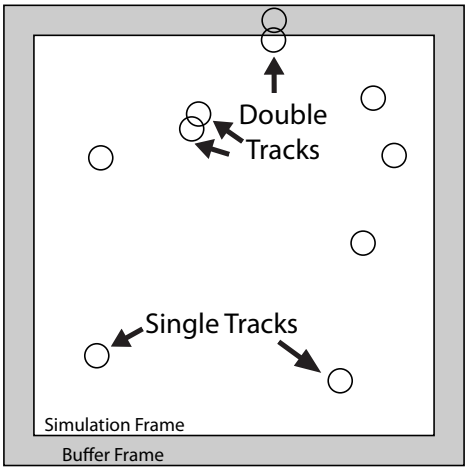

Figure 6: An example simulation frame with six single tracks and three double tracks.

The problem is polynomial run time in the total number of tracks, increment dN, and the total fraction of tracks overlapping. While polynomial algorithms are in general computationally easy, the large Ns required can cause long run times. For that reason the simulation plane is split into multiple areas for parallel processing.

4. Simulation results

In this section, we present simulation results under various conditions to both illustrate the versatility of the code as well as examine properties of track overlap in CR-39 and other similar detectors. For the former, we first show the fractions F_n for $n = 1, 2, 3$ and $n \geq 4$ versus track density χ in Fig. 7. We can see that the track overlap becomes significant when χ is a few tenths. The parameter χ is 'universal' for any diameter and fluence combination through $\chi \equiv \eta \times (\pi \bar{D}^2)$, so the curves in Fig. 7 vs χ apply to any narrow distribution.

In this problem a 'narrow' distribution refers to the case when σ/D is small compared to 1, as in Section 2. Since the Monte Carlo code can sample arbitrary distributions we can explore this regime with Gaussian distributions. For example, for $D = 6$ μm we take $\sigma = 0, 0.5, 1.0, 2.0$ μm and plot F_1 and F_2 versus χ, Fig. 8, we can clearly see that there is no effect on $F_1(\chi)$ for Gaussian distributions up to $\sigma/D \sim 1/3$. However, if we instead plot $F_2(\chi)$ we can see deviations for χ of order unity between the various distributions. We therefore conclude that the distribution width is a second-order effect in that it does not change the fraction of tracks that are non-overlapping for reasonable χ. For higher n there is an effect for $\sigma/D \gtrsim 0.1$

Similar effects can result from non-Gaussian diameter distributions, which occur in real data. Fig. 9 shows a track diameter distribution from ~ 3 MeV protons incident on a CR-39 detector. There are small components in the distribution at much larger track diameters than the mean, at $D \sim 18$ and 27 μm.

The track overlap for the distribution in Fig. 9 was simulated when considering the whole distribution and a Gaussian fit to the prominent peak at $D \sim 9$ μm. The results are shown in Fig. 10. Similarly to the effect of the distribution standard deviation we see no difference in the fraction of single tracks for the raw distribution compared to the Gaussian distribution. However, the double track fraction F_2 shows a deviation indicating that non-Gaussian distributions are also a second-order effect changing overlap fractions F_n for $n \geq 2$.

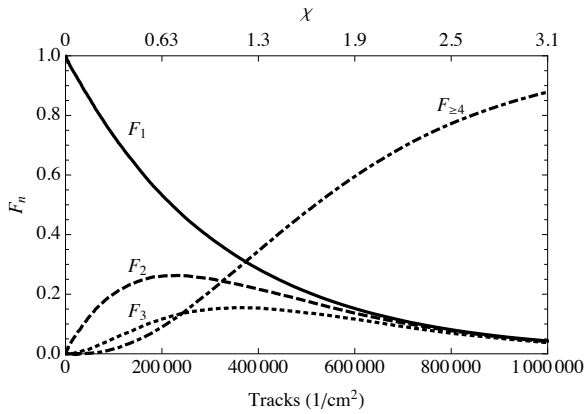

Figure 7: F_n versus track density for 10 μm tracks and $n = 1$ (solid line), $n = 2$ (dashed line), $n = 3$ (dotted line), and a sum of all $n \geq 4$ (dot-dashed line). When plotted versus *chi* the shape of the curve is 'universal' for any diameter through the relation $\chi \equiv \eta \times (\pi \bar{D}^2)$. In Fig. 3, we can see that the analytic model is only valid until $\chi \sim 0.25$, compared to the Monte Carlo code which can be run to high χ.

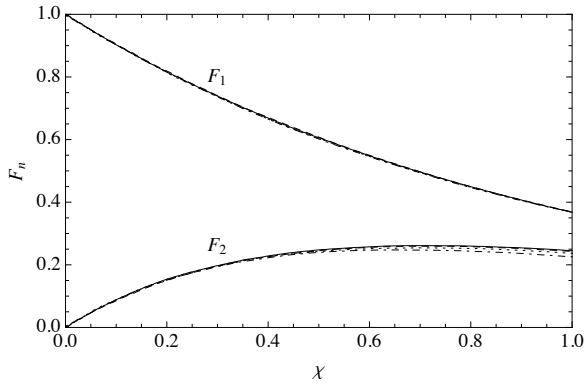

Figure 8: F_1 and F_2 vs χ for track $D = 6$ μm and $\sigma = 0$ (solid line), 0.5 (dashed line), 1.0 (dotted line), and 2.0 (dot-dashed line) μm. The curves overlap significantly for F_1, and show small deviation with σ at $\chi \sim 1$.

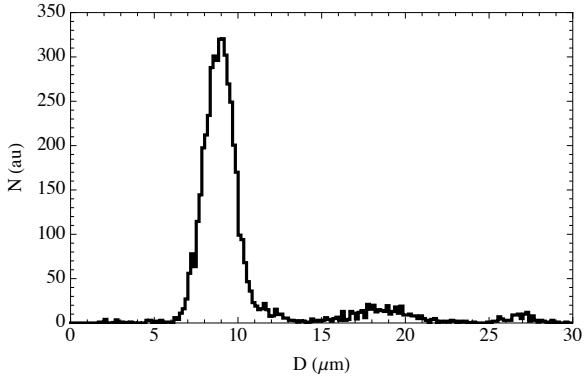

Figure 9: A diameter distribution from real CR-39 data with a primary proton signal at $D \sim 9$ μm and weaker non-Gaussian components at larger diameters ($D \sim 18$ and 27 μm).

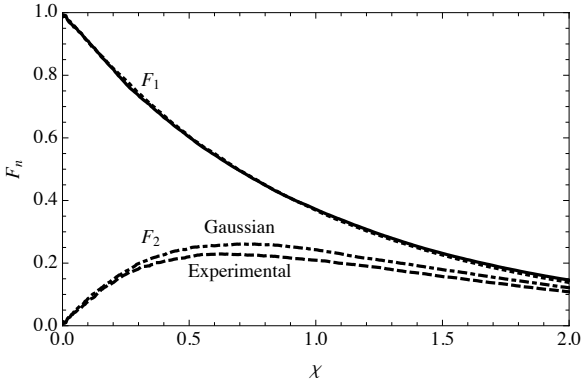

Figure 10: Simulations of F_1 and F_2 for the experimental diameter distribution (solid and dashed lines, respectively) and a Gaussian fit to the primary component at $D \sim 9$ μm (dotted and dot-dashed, respectively).

5. Post-hoc overlap correction algorithm

The Monte Carlo simulation is also used for a post-hoc correction of track overlap in data. In experimental data it is difficult to analyze an overlapping track structure due to complicated geometry and the stochastic track placement (e.g. see Fig. 1). If the number of non-overlapping tracks is known, on the other hand, it can be related via theory or simulation to the total number of tracks (see Sec. 2 or 4).

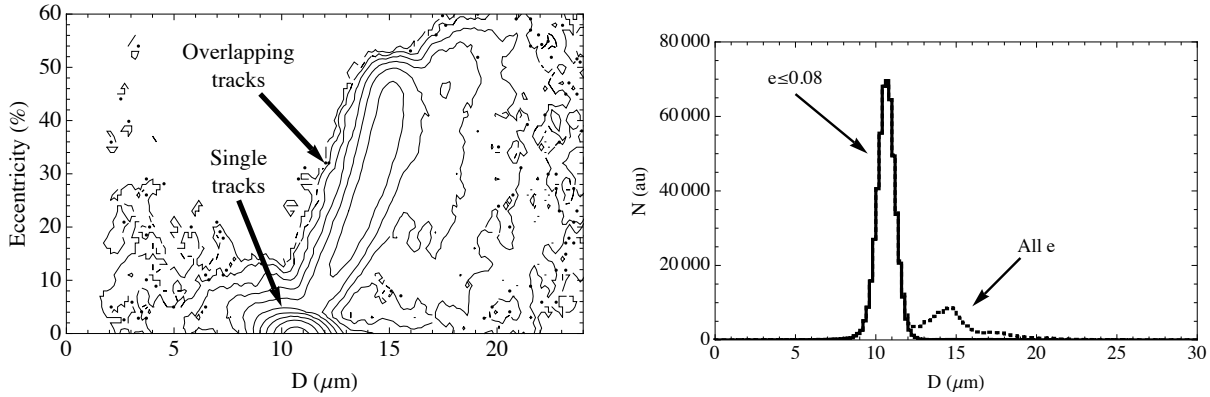

Figure 11: (a) Contour plot of number of tracks versus track eccentricity and diameter, for overlapping data etched to 6 hours. The diameter is defined as $D = 2\sqrt{A/\pi}$ where A is the total measured track area. Single tracks are visible near zero eccentricity (perfectly round) and $D \sim 11$ μm while overlapping tracks have more eccentricity and larger diameters. The ratio of adjacent contours is 2. (b) Diameter histogram for the same data, with an eccentricity limit of 8% (solid) and without limit (dotted). The eccentricity is defined as for a geometric ellipse; $e \leq 0.08$ means that tracks are only accepted if they are between perfectly circular ($e = 0$) and 8% out of round ($e = 0.08$).

To discriminate against overlapping tracks, which are still detected by the automated optical microscope system used to process CR-39 [12], it is necessary to discriminate between single and overlapping tracks in this method. In principle this can be done by using the track eccentricity information; e.g. two overlapping non-concentric tracks will form a quasi-elliptical shape with non-zero eccentricity and larger diameter than

a single track. As a demonstration, Fig. 11 shows a contour plot of CR-39 data with overlap. The single tracks are clustered at $D \sim 11$ μm and eccentricity of about a few percent. The overlapping tracks appear at larger diameter and eccentricities of several tens of percent. Additionally, we note that inferred diameter is proportional to eccentricity as expected from geometry. In this case, the data could be limited to eccentricities below $8 - 10\%$ to reject overlapping tracks while retaining single tracks.

Once the data is discriminated to single tracks only, the measured track distribution is used as a source function in the Monte Carlo simulation. The code then incrementally increases the track fluence until it matches the observed fluence of single tracks, at which point the code reports the total fluence necessary to match the data.

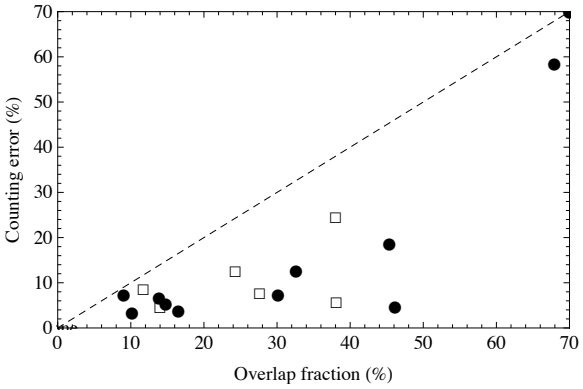

Figure 12: Experimental test of the algorithm performance. Data points are plotted as inferred counting error vs overlap fraction. Two datasets are shown: accelerator DD-p (circles) and OMEGA D^3He-p (open squares). A naïve counting scheme, without overlapped tracks counted, would lie on the 45° line (dashed).

Experimental tests of this method have been performed using a linear electrostatic ion accelerator (LEIA) fusion products source at MIT [22, 23], and with capsule implosions at the OMEGA laser [18]. In the accelerator experiment we used energetic protons from the reaction

$$\mathrm{D} + \mathrm{D} \rightarrow \mathrm{T}(1.01\ \mathrm{MeV}) + \mathrm{p}(3.02\ \mathrm{MeV}), \tag{10}$$

and in the OMEGA experiments from the reaction

$$\mathrm{D} + {}^3\mathrm{He} \rightarrow {}^4\mathrm{He}(3.6\ \mathrm{MeV}) + \mathrm{p}(14.7\ \mathrm{MeV}), \tag{11}$$

to expose CR-39 samples to various proton fluences. The CR-39 was etched for a short enough period of time that there was minimal overlap and the fluence recorded. We then etched the CR-39 further until significant overlap occured, and rescanned the same area again. This allows an accurate determination of the counting precision with induced track overlap.

The results of this experiment are shown in Fig. 12, plotted as the measured counting error in the overlapping data versus the fraction of tracks overlapping. In the naïve case, with all overlapping tracks thrown away and no correction, the trend would be a 45° line (dashed line). For relatively low amounts of overlap $10 - 20\%$, the algorithm has a counting error $< 10\%$. For higher overlap fractions $\sim 30 - 45\%$ the counting error increases to $\sim 10 - 20\%$. Finally, at very high overlap fractions (70%) the algorithm breaks down and the counting error becomes very large.

The algorithmic accuracy is primarily limited by the single vs overlapping track discrimination (via eccentricity cuts in the CR-39 analysis), as well as statistics in determining fluence and diameter distributions in both the data and calculation. For these reasons the current results are a limitation of the method.

By comparison to Fig. 7, where the overlap fractions are plotted versus fluence, we can see that in applications were $\sim 10\%$ counting accuracy is acceptable this technique can extend the upper fluence limit of CR-39 by about a factor of $3 - 4$.

6. Conclusions

The solid-state nuclear track detector CR-39 is used in various diagnostics at laser ICF facilities, where high track fluences are easily achievable. Previous counting techniques were limited to regimes in which the physical overlap of particle tracks was small, which defined the upper limit of dynamic range for many of these diagnostics. In the low-overlap regime the overlapping fraction of tracks scales as $\chi \equiv \eta \times (\pi \bar{D}^2)$ where η is the density of tracks and $\bar{D}$ is the average track diameter, derived in a simple theory. A Monte Carlo simulation code has been developed to study the effects of track overlap in these detectors under various scenarios. Illustrative examples of simulation results are presented. We report on a post-hoc overlap correction algorithm, which uses Monte Carlo simulations to correct for overlap in CR-39 data based on matching simulated single track results to the data. In applications where counting accuracy $\sim 10\%$ is acceptable, this technique can extend the upper fluence limit by a factor of $3-4$x. Future work will focus on the development of a new algorithm to recognize overlapping tracks based on shape during the optical microscope scan, which will allow for diameter measurements and more accurate counting in high-fluence scenarios.

For applications such as high-precision counting (to a few percent for MRS data) or diameter identification of overlapping tracks for complicated distributions (i.e. Wedge Range Filter [12] data) another technique is required. The future work of this project includes the development of an algorithm to recognize overlapping tracks during the optical microscope scan by the track shape. Benchmarking this algorithm will then allow its application to diagnostics at laser fusion facilities. We will also study the response of CR-39 track detectors at short etch times ($1-2$ hours, versus typical 6) to characterize the minimum etch time necessary to distinguish data from noise; this short-etch technique will also be useful for extending the upper fluence range of these detectors.

7. Acknowledgments

The authors thank the engineering and operations staff at the OMEGA facility for their support, as well as J. Schaeffer, R. Frankel, and E. Doeg for contributing to the CR-39 processing.

The work described here was done in part for the first authors's Ph.D. thesis and was supported in part by the U.S. DoE (DE-FG52-09NA29553), the LANL ICF Program, LLNL (B580243), LLE (414090-G), the Fusion Science Center at the University of Rochester (415023-G and DE-FC02-04ER54789), and the National Laser Users Facility (DE-NA0000877 and DE-FG03-03SF2269). A. Zylstra is supported by the DoE NNSA Stewardship Science Graduate Fellowship (DE-FC52-08NA28752).

Appendix A. Diameter distribution evolution

As an example, we provide contour plot of number of tracks versus track eccentricity and diameter as well as diameter histograms for a dataset with overlap induced via progressive etches. Filters are used to reduce the proton energy from 14.7 MeV (undetectable with CR-39) to ~ 4 MeV, which is in the detectable regime. All CR-39 used in this study was etched with a 6 molar NaOH solution at 80° C.

Appendix B. Fluence Examples

For reference, we present example microscope images for various fluences of DD-p on CR-39 in Fig. B.15.

Appendix C. Shot Numbers

Facility shot numbers (A denotes MIT linear electrostatic ion accelerator, Ω denotes the OMEGA laser facility) for all data given in this paper are tabulated in Table C.2.

[1] D. Young, Nature (1958).
[2] E. Silk, R. Barnes, Philosophical Magazine 4 (1959) 970–972.

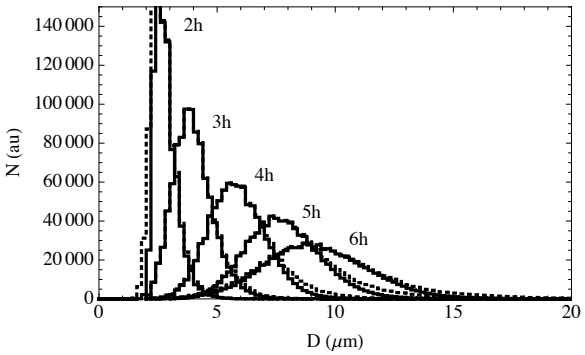

Figure A.13: Diameter distributions for D^3He-p data etched to 2-6h. Solid traces are for eccentricities less than 15%, while dotted curves are summed over all eccentricities. The data presented in this plot is the same as in Fig. A.14.

Figure	Shot Number
1	A2010020104
9	A2009102201
11	A2010020104
12	A2010020101-4 A2010021701-3 Ω62407-8
A.13	Ω62407
A.14	Ω62407
B.15	A2010020102-4

Table C.2: Shot numbers for experimental data shown in each figure.

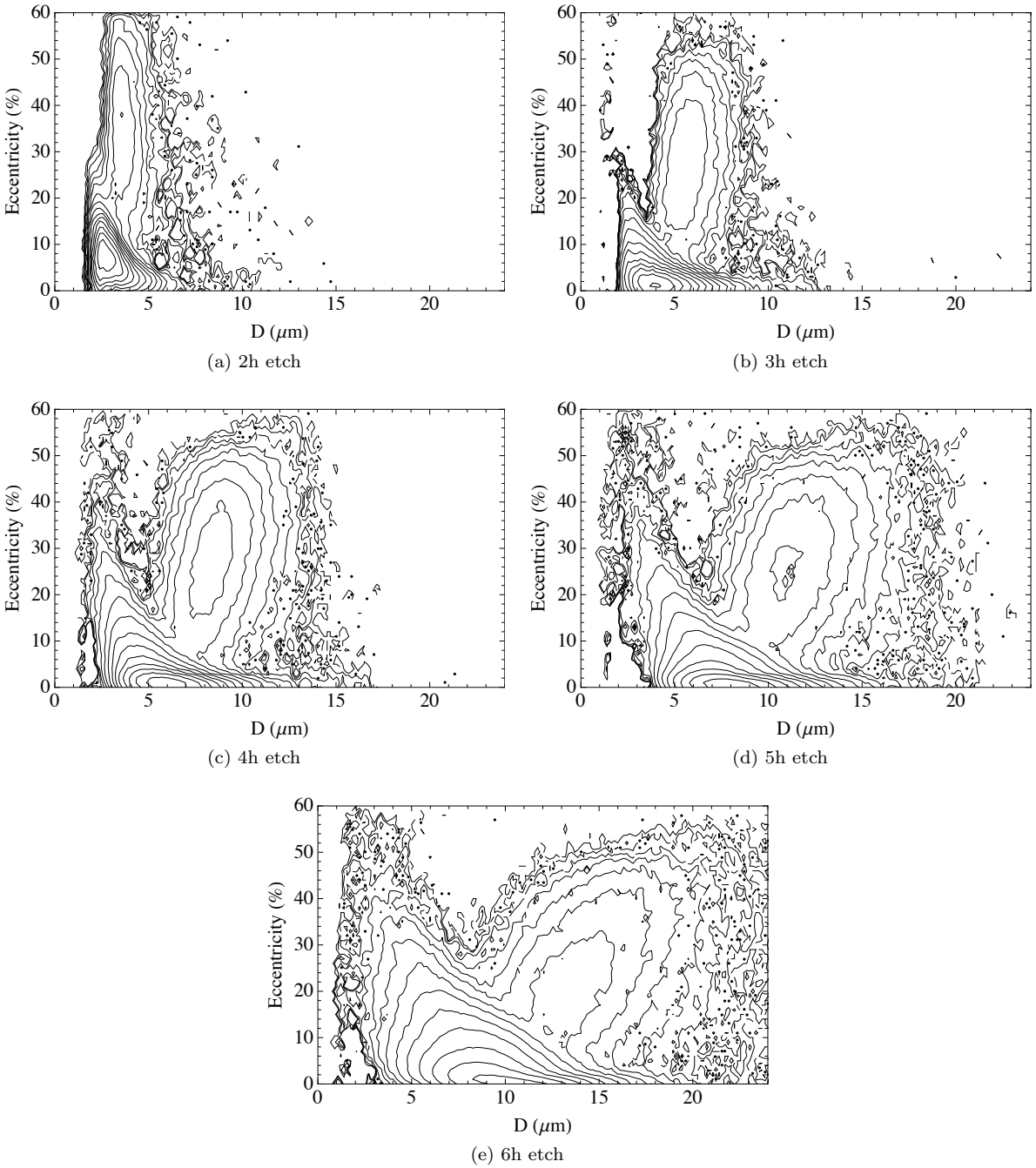

(a) 2h etch

(b) 3h etch

(c) 4h etch

(d) 5h etch

(e) 6h etch

Figure A.14: Contour plots of number of tracks versus track eccentricity and diameter, for overlapping D^3He-p data etched to 2-6 hours. Single tracks are visible near zero eccentricity (perfectly round) while overlapping tracks have more eccentricity and larger diameters. The ratio of adjacent contours is 2. The data presented in this plot is the same as in Fig. A.13.

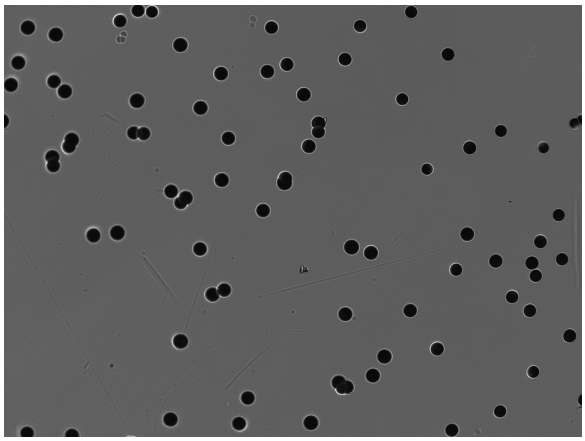

(a) $\eta = 4.4 \times 10^4$ p/cm^2, or $\chi = 0.16$

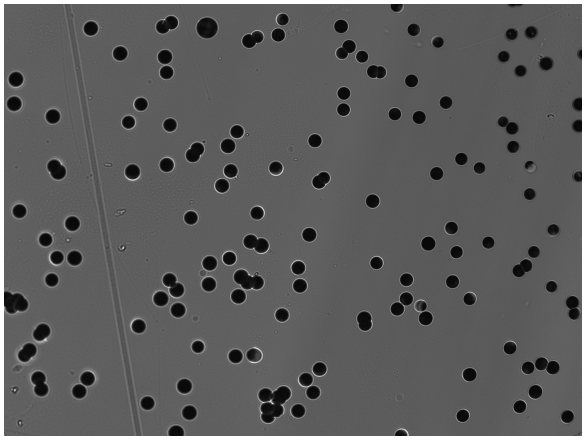

(b) $\eta = 8.9 \times 10^4$ p/cm^2, or $\chi = 0.33$

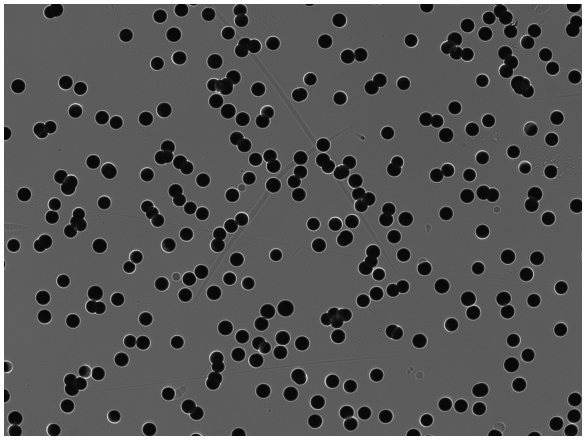

(c) $\eta = 1.8 \times 10^5$ p/cm^2, or $\chi = 0.63$

Figure B.15: Varying fluences of 3 MeV DD-p, CR-39 with overlap observable after being etched for 6 hours. The image was taken with an optical microscope system with a frame area of 1.36×10^{-3} cm^2 (431μm $\times$ 315.5μm). 25μm Aluminum filtering was used to remove couplementary particles (T, ^{3}He, ^{4}He) from DD and D^{3}He fusion. Neutrons from DD fusion are also incident on the CR-39, but the detection efficiency for neutrons (due to scattered protons in the CR-39) is 10^{-4} below the proton detection efficiency and the neutrons are therefore negligible in this work.

[3] R. Fleischer, P. Price, R. Walker, Nuclear tracks in solids: principles and applications, University of California Press, 1975.
[4] S. Durrani, R. Bull, Solid state nuclear track detection, Pergamon Books Inc., Elmsford, NY, 1987.
[5] A. Fews, D. Henshaw, Nuclear Instruments and Methods in Physics Research 197 (1982) 517–529.
[6] N. Sinenian, et al., To be submitted to Review of Scientific Instruments (2011).
[7] J. Lindl, Physics of Plasmas 2 (1995) 3933.
[8] S. Kacenjar, S. Skupsky, A. Entenberg, L. Goldman, M. Richardson, Phys. Rev. Lett. 49 (1982) 463–467.
[9] D.G. Hicks, Charged-Particle Spectroscopy: A New Window on Inertial Confinement Fusion, 1999.
[10] C. Li, D. Hicks, F. Séguin, J. Frenje, R. Petrasso, J. Soures, P. Radha, V. Glebov, C. Stoeckl, D. Harding, et al., Physics of Plasmas 7 (2000) 2578.
[11] D. Hicks, C. Li, F. Séguin, J. Schnittman, A. Ram, J. Frenje, R. Petrasso, J. Soures, D. Meyerhofer, S. Roberts, et al., Physics of Plasmas 8 (2001) 606.
[12] F. Séguin, J. Frenje, C. Li, D. Hicks, S. Kurebayashi, J. Rygg, B. Schwartz, R. Petrasso, S. Roberts, J. Soures, et al., Review of Scientific Instruments 74 (2003) 975.
[13] J. Frenje, K. Green, D. Hicks, C. Li, F. Séguin, R. Petrasso, T. Sangster, T. Phillips, V. Glebov, D. Meyerhofer, et al., Review of Scientific Instruments 72 (2001) 854.
[14] J. Frenje, C. Li, F. Séguin, D. Hicks, S. Kurebayashi, R. Petrasso, S. Roberts, V. Glebov, D. Meyerhofer, T. Sangster, et al., Review of Scientific Instruments 73 (2002) 2597.
[15] C. Li, F. Séguin, J. Frenje, J. Rygg, R. Petrasso, R. Town, P. Amendt, S. Hatchett, O. Landen, A. Mackinnon, et al., Review of Scientific Instruments 77 (2006) 10E725.
[16] J. Rygg, F. Seguin, C. Li, J. Frenje, M. Manuel, R. Petrasso, R. Betti, J. Delettrez, O. Gotchev, J. Knauer, et al., Science 319 (2008) 1223.
[17] C. Li, F. Seguin, J. Frenje, M. Rosenberg, R. Petrasso, P. Amendt, J. Koch, O. Landen, H. Park, H. Robey, et al., Science 327 (2010) 1231.
[18] T. Boehly, D. Brown, R. Craxton, R. Keck, J. Knauer, J. Kelly, T. Kessler, S. Kumpan, S. Loucks, S. Letzring, et al., Optics communications 133 (1997) 495–506.
[19] G. Miller, E. Moses, C. Wuest, Nuclear fusion 44 (2004) S228.
[20] S. Gaillard, J. Fuchs, N. Renard-Le Galloudec, T. Cowan, Review of scientific instruments 78 (2007) 013304.
[21] D. Gautier, J. Kline, K. Flippo, S. Gaillard, S. Letzring, B. Hegelich, Review of Scientific Instruments 79 (2008) 10E536.
[22] S. McDuffee, J. Frenje, F. Séguin, R. Leiter, M. Canavan, D. Casey, J. Rygg, C. Li, R. Petrasso, Review of Scientific Instruments 79 (2008) 043302.
[23] N. Sinenian, et al., to be submitted to Rev. Sci. Instrum. (2012).
[24] T. Yamauchi, Radiation measurements 36 (2003) 73–81.
[25] J. Frenje, D. Casey, C. Li, F. Séguin, R. Petrasso, V. Glebov, P. Radha, T. Sangster, D. Meyerhofer, S. Hatchett, et al., Physics of Plasmas 17 (2010) 056311.